Stabilization of Chemical-Vapor-Deposition-Grown WS$_2$ Monolayers at Elevated Temperature with Hexagonal Boron Nitride Encapsulation

Xiang Hua, Datong Zhang, Bumho Kim, Dongjea Seo, Kyungnam Kang, Eui-Hyeok Yang, Jiayang Hu, Xianda Chen, Haoran Liang, Kenji Watanabe, Takashi Taniguchi, James Hone, Young Duck Kim, and Irving P. Herman*

Read Online

ACCESS | Metrics & More | Article Recommendations | SI Supporting Information

ABSTRACT: Chemical vapor deposition (CVD)-grown flakes of high-quality monolayers of WS$_2$ can be stabilized at elevated temperatures by encapsulation with several layer hexagonal boron nitride (h-BN), but to different degrees in the presence of ambient air, flowing N$_2$, and flowing forming gas (95% N$_2$, 5% H$_2$). The best passivation of WS$_2$ at elevated temperature occurs for h-BN-covered samples with flowing N$_2$ (after heating to 873 K), as judged by optical microscopy and photoluminescence (PL) intensity after a heating/cooling cycle. Stability is worse for uncovered samples, but best with flowing forming gas. PL from trions, in addition to that from excitons, is seen for covered WS$_2$ only for forming gas, during cooling below ∼323 K; the trion has an estimated binding energy of ∼28 meV. It might occur because of doping level changes caused by charge defect generation by H$_2$ molecules diffusing between the h-BN and the SiO$_2$/Si substrate. The decomposition of uncovered WS$_2$ flakes in air suggests a dissociation and chemisorption energy barrier of O$_2$ on the WS$_2$ surface of ∼1.6 eV. Fitting the high-temperature PL intensities in air gives a binding energy of a free exciton of ∼229 meV.

KEYWORDS: WS$_2$, monolayer, transition-metal dichalcogenide (TMD) monolayers, photoluminescence, h-BN encapsulation, elevated temperature, excitons, trions
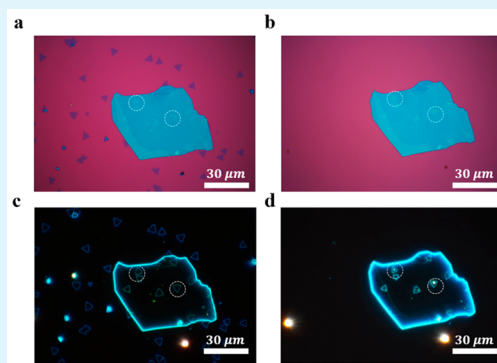
INTRODUCTION

Layered transition-metal dichalcogenides (TMDs) have attracted much attention because of their electronic and optical properties.[1] One of the distinctive properties of several TMDs is the appearance of a direct band gap transition in the monolayer, rather than the indirect gap in the bulk material, and this can provide strong luminescence in the visible.[2,3] This can lead to several important applications in optoelectronic devices,[4,5] including photodetectors,[6,7] and light-emitting diodes (LEDs).[8]

One of the major obstacles in using TMDs to realize these applications at elevated temperature is their stability. Bulk TMDs are known to be relatively unstable at higher temperatures, in oxygen-containing media, in the presence of inert gases, and under vacuum.[9,10] Some recent work shows the limited stability of few-layer TMDs at elevated temperatures,[11−15] but less is known about the stability of monolayer TMDs under various environmental conditions at high temperature. It is known that potential microscopic structural transitions, defect formation, and substrate absorption resulting in trap states and undesirable doping can occur at higher temperatures, as well as decomposition.[11−14] The existence of

imperfections can significantly degrade luminescence quantum yields and the on/off ratios of field-effect transistors (FETs).[16] Therefore, understanding TMD stability and developing effective passivation methods of TMDs are essential for high-performance applications at elevated temperatures.

h-BN (hexagonal boron nitride) is known to be thermally stable up to ∼1800 K.[17] h-BN encapsulation is now widely used for the passivation of graphene and 2D semiconductors, such as for improving luminescence efficiency and achieving high electronic quality.[18,19] In this study, we learn that WS$_2$ monolayers can be stabilized at high temperatures by using h-BN encapsulation. We investigated the stability and resulting quality of h-BN encapsulated and uncovered regions of WS$_2$ monolayers, grown by chemical vapor deposition (CVD), by using *in situ* optical photoluminescence (PL) and other optical
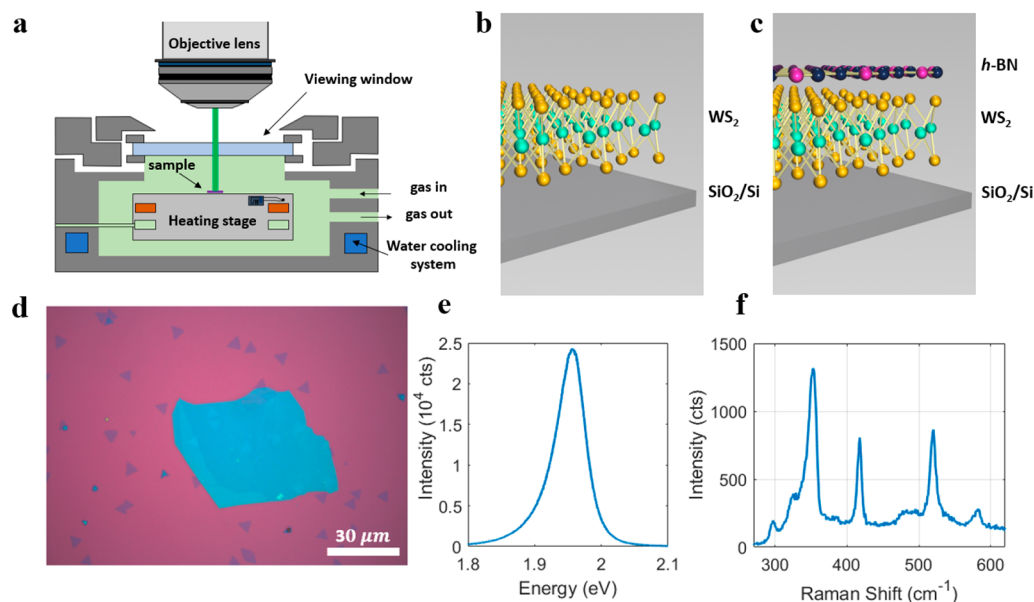
**Figure 1.** (a) Schematic depiction of a sample placed in a Linkam cell where the temperature and environment are controlled and materials processing is monitored in real time. (b) Crystal structure of CVD-grown monolayer WS_2 on a SiO_2/Si substrate. (c) Crystal structure of a van der Waals stacked sample that is composed of monolayer WS_2 encapsulated with h-BN on a SiO_2/Si substrate. (d) Optical image showing monolayer CVD-grown WS_2 on a SiO_2/Si substrate, with a few of the flakes encapsulated by h-BN (and are not seen). Monolayer WS_2 is characterized in air by (e) PL measurement and (f) Raman scattering (with the 520 cm^{-1} peak due to Si), at 300 K.
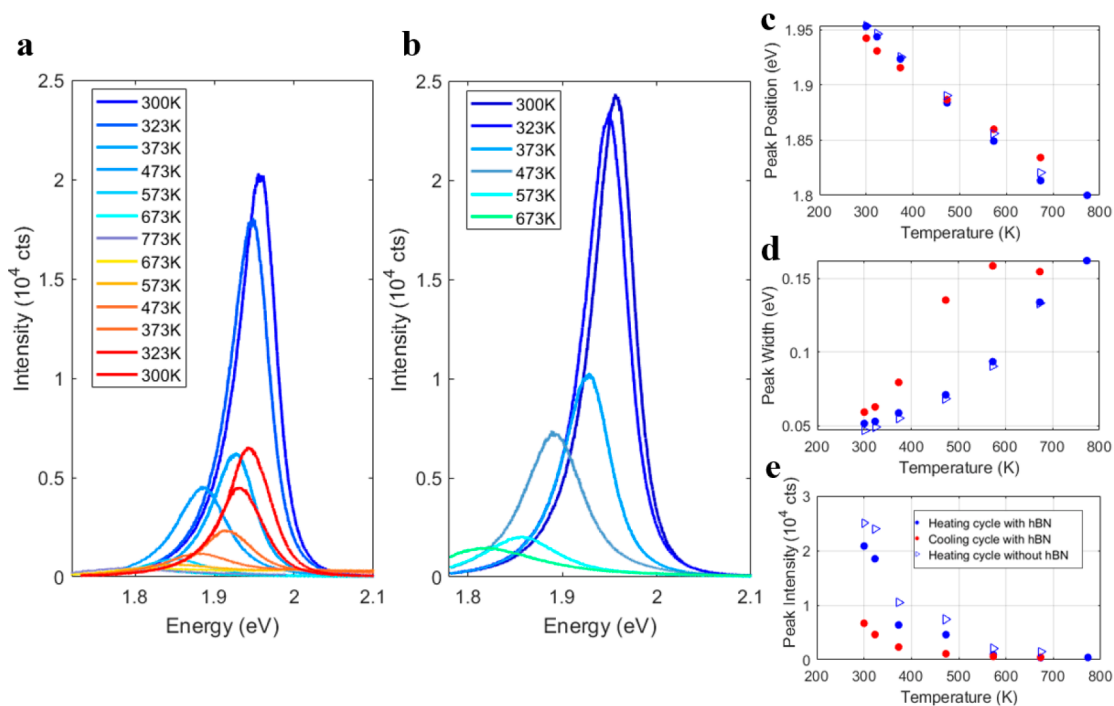

Figure 2. *In situ* PL spectra of CVD-grown WS_2 flakes (a) covered, during heating, and (b) uncovered by h-BN, during the heating/cooling cycle in ambient air, at different temperatures in real time. (c) Positions, (d) fwhms, and (e) peak intensities of the PL peak of the h-BN-covered WS_2 flakes and uncovered flakes versus temperature (with symbols defined in (e)).

measurements at different stages of the heating/cooling cycles and in the presence of different gas environments.

■ EXPERIMENTAL SECTION

The monolayer WS_2 was grown on a 285 nm SiO_2/Si substrate by CVD,[20] and then characterized by optical microscopy, which showed resulting equilateral triangle flakes. The length of the side of the flake was ~5−30 μm. h-BN flakes of near quadrilateral shape with a longest

side length of 50−100 μm, and much larger than the corresponding WS_2 flake dimensions, were then exfoliated onto a SiO_2/Si substrate, and their thickness and uniformity were determined by atomic force microscopy (AFM). Standard transfer methods were used to transfer h-BN flakes to the top of the $WS_2/SiO_2/Si$, by first picking up the h-BN layers with a PPC/PDMS slide (poly(propylene) carbonate (PPC), polydimethylsiloxane (PDMS))[21] and then transferring them on top of the monolayer WS_2. Then the chips were put in acetone
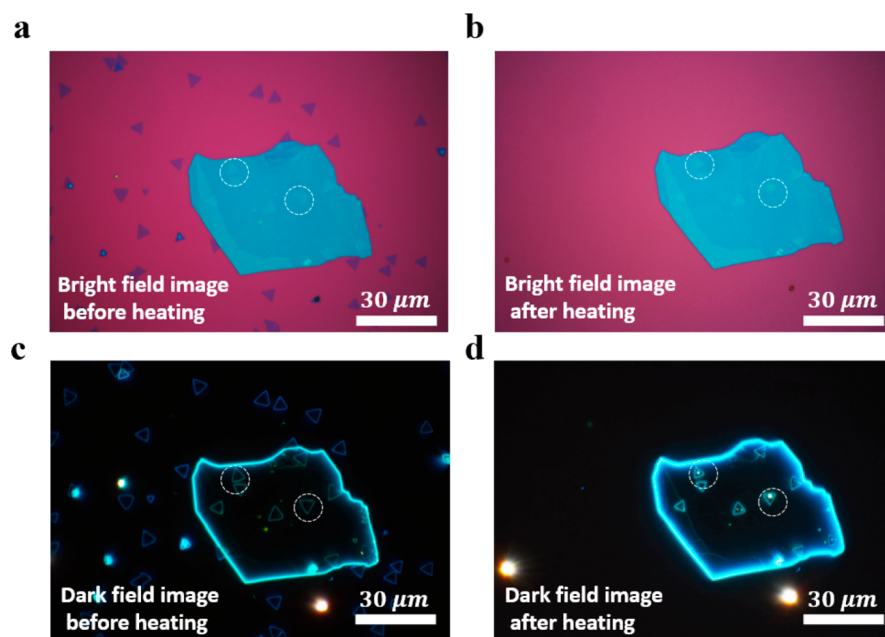
Figure 3. (a) Optical image of triangular monolayer CVD-grown WS$_2$ flakes on a SiO$_2$/Si substrate, with several of the flakes covered by h-BN (light blue). These covered flakes are barely visible here, and the two of them that are clearly seen to have bluish spots in (b) and (d) are encircled in each image. (b) Optical image of the same sample after heating to 773 K in ambient air and cooling to room temperature. (c) and (d) are dark-field microscope images showing the same samples as in (a) and (b), and the outline of the h-BN is also seen in both. After heating, the uncovered WS$_2$ flakes are seen to have decomposed, whereas the covered ones remain. The optical image exposure in (d) is longer than that in (c) to enable seeing the bluish centers in the center of covered WS$_2$. All images are at room temperature.

overnight and the remaining PPC residue was cleaned with isopropyl alcohol.

Optical analysis of the WS$_2$ occurred with *in situ* control of the temperature and environment in a Linkam cell (LINKAM THMS 600) (Figure S1 in the Supporting Information). A schematic view of the *in situ* optical measurements with control of the temperature and gas environment is given in Figure 1a. Two regions on the chip were probed in the optical measurements: the CVD-grown monolayer WS$_2$ with h-BN encapsulation, called the covered regions, and the bare monolayer WS$_2$ on the substrate, called the uncovered regions. Schematic views of the crystal structure in the regions are shown in Figure 1b,c. The optical image of the entire sample is shown in Figure 1d.

In situ PL measurements using a continuous-wave argon ion laser (514.5 nm) were performed over a range of temperatures in real time first in ambient air. The temperature was increased from room temperature to 773 K (and no higher because the uncovered sample decomposed at this temperature), with a heating rate of 50 K/min to a given target temperature, at which PL was measured after waiting 10 min to ensure thermal equilibrium, before further heating continued; the same procedure was followed during cooling. Signals were captured by a cryogenically cooled silicon CCD detector (Princeton Instruments Spec-10:400B). For confirmation that the WS$_2$ flakes did not macroscopically degrade and were well preserved after sample fabrication, the monolayer WS$_2$ flakes were characterized by room-temperature Raman scattering and PL before the start of each run, as seen in Figure 1e,f for ambient air, in Figure S2 for flowing N$_2$, and in Figure S3 for flowing forming gas in the Supporting Information.

Figure 2a,b shows the temperature-dependent PL spectra of WS$_2$ respectively in a covered and an uncovered region. The sample was heated in ambient air from room temperature to 773 K and then cooled down to room temperature, monitored by *in situ* PL at each targeted temperature. The PL evolved in covered and uncovered regions similarly from room temperature to 673 K. Above 673 K, the uncovered regions of the sample started to decompose and totally disappeared when the temperature approached 773 K, as seen by optical microscopy (Figure 3a,b). (This is why 673 K is the highest temperature with measurable PL in the uncovered regions.) In

contrast, in covered regions WS$_2$ was still observable and still showed strong PL emission. However, the PL signals of the covered sample did not return to their initial values after cooling to room temperature (Figure 2e); the integrated PL intensities were ~63% lower than those at the beginning. This could be associated with the spot features that formed at the center of the covered WS$_2$ triangles, as observed by optical microscopy in Figure 3c,d, that indicates some degradation.

In the h-BN-covered region, the PL peak position of monolayer WS$_2$ follows similar trends in the heating and in the cooling cycles, but they are not identical (Figure 2c). The peak is located at 1.954 eV at room temperature at the beginning of the run and at 1.942 eV after it. This small red shift of 12 meV could be caused by an increase in the biaxial in-plane tensile strain by ~0.12% (see below).[22−25] As seen in Figure 2d, the fwhm peak width was 51.3 meV before the heating cycle and 59.1 meV after cooling to room temperature. This broadening, along with the PL intensity decrease, might mean the exciton lifetime has decreased. Peak width broadening might result from impurity or defect formation leading to faster nonradiative recombination or from increased local inhomogeneity during heating.

The optical images of the sample in ambient air before and after the heating/cooling to 773 K are compared in Figure 3. Figure 3a,c shows the bright and dark field optical images at room temperature before the cycle. The triangles are monolayer WS$_2$ grown by CVD and the big blue quadrilateral-shaped flake is the several-layer h-BN on top of the WS$_2$. The micrograph of the same sample region after the heating/cooling cycle in Figure 3b shows three things. First, all monolayer WS$_2$ in the uncovered region has totally decomposed, which is consistent with the *in situ* PL measurements presented in Figure 2b. Second, the shape and area of the monolayer WS$_2$ flakes in the covered region remain unchanged, indicating that the WS$_2$ flakes did not apparently decompose at 773 K because of the protection by h-BN encapsulation. Third, when the dark-field optical images in parts (c) and (d) of Figure 3 are compared, a blueish spot appears at the center of each triangular, a WS$_2$ flake in the covered region after the heating/cooling cycle in air; the two flakes where this spot is seen clearest are encircled. As noted, these spots might be one of the reasons why the PL intensity decreases in Figure 2e. These spots also appear in the bright-field image in Figure 3b.
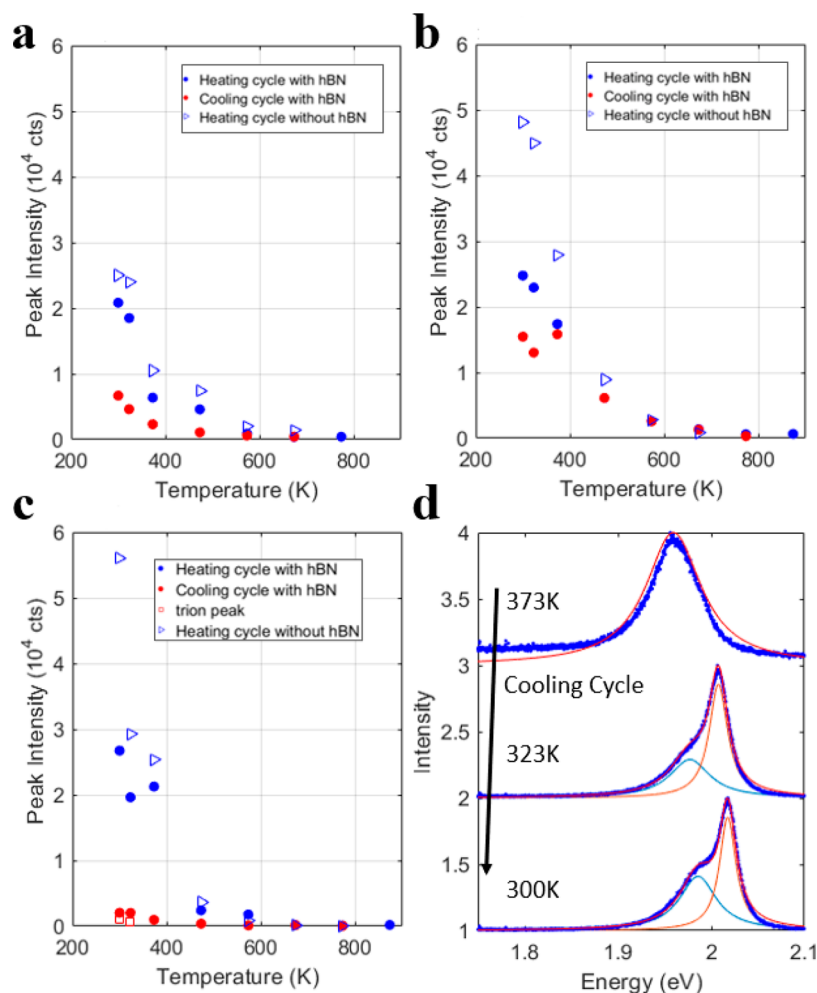
Figure 4. (a) PL exciton peak intensity of *h*-BN-covered WS_2 flakes and uncovered flakes versus temperature for (a) ambient air, (b) flowing N_2 at 1 atm, and (c) forming gas flowing (95% N_2, 5% H_2) at 1 atm. In (c) the PL trion peak intensity is also plotted, for the trion peak that is seen near the end of the cooling phase of the heating/cooling cycle, as resolved in (d) (where the trion peak is blue and exciton peak is red). In forming gas, uncovered WS_2 survives above 673 K and still shows strong PL and starts to decompose above 773 K.

Covering monolayer WS_2 with *h*-BN provides some passivation of monolayer WS_2 in air to ~773 K, but it is not perfect, as seen by the decrease of the PL intensity. Therefore, such PL measurements were repeated during heating/cooling cycles, during which 20 sccm N_2 (at 1 atm) flowed in the chamber (Figure 4b) and then repeated again with forming gas (95% N_2, 5% H_2) (Figure 4c), but now with heating to 873 K; for reference, the PL data for ambient air are shown in Figure 4a. For flowing N_2, the PL from covered and uncovered regions were similar from room temperature until 673 K. The uncovered sample began to disappear when the temperature was above 673 K and disappeared totally at 773 K. Covered WS_2 still showed strong PL emission to 873 K. After this entire heating/cooling cycle, the integrated PL intensities of the covered region were ~47% lower than those at the beginning and there was a PL blue shift of ~11 meV.

Then the measurement was repeated with flowing forming gas and heating to 873 K. The temperature-dependent PL intensity is shown in Figure 4c. Interestingly, the uncovered WS_2 then started to decompose at 773 K, and totally disappeared when the temperature approached 873 K. The uncovered WS_2 survives to a higher temperature in a forming gas environment than in air or N_2, perhaps because WS_2 decomposition is related to the oxygen and water vapor in the surrounding area, and forming gas helps reduce oxidation. With WS_2 covered by *h*-BN, the sample and the observed PL remain to the high temperature of 873 K. Trion peaks appear only for these covered samples and only with flowing forming gas, during cooling starting at

323 K, and they are strong at room temperature. This suggests unintentional charges are induced at high temperature and the doping level of the covered WS_2 changes. Finally, after the entire heating/cooling cycle, the integrated PL signals of the covered region are ~96% lower than those at the beginning of the cycle. (Including only excitonic (and not trion) emission, the decrease in the integrated PL signal is 98%.) This suggests that covered WS_2 becomes more damaged than that with heating in air (to 773 K) or flowing N_2 (to 873 K). Therefore, *h*-BN encapsulation passivates the covered WS_2 the least with forming gas present. The PL peak was blue-shifted by 67 meV, which also suggests damage (see below). The Raman spectra in Figure S4 show no evidence of sulfur-terminated surfaces after heating in forming gas, with the formation of thiols, which could be one route toward passivation; this route also appears to be unlikely because there is no excess sulfur for this to occur.[26,27] They also show no evidence of the partial reduction of the SiO_2 (due to the H_2 in forming gas), which could lead to the charges needed for trion formation—but these levels may be too small to be seen by Raman scattering.

Therefore, the best passivation occurred for covered samples with flowing N_2, and the best for uncovered samples was with flowing forming gas.

Because heating caused the least damage in covered WS_2 with flowing N_2, bright-field micrographs of the sample before and after heating were retaken for flowing N_2 up to 873 K, as with that for air in Figure 3a,b with heating to 773 K, as shown in Figure S5 in the

Supporting Information. Unlike for air, no spots in the center of the WS$_2$ were seen after heating, which also indicates less damage.

RESULTS AND DISCUSSION

Gao et al. used XPS analysis to show that sulfur oxide does not form when WS$_2$ is in air, and therefore WS$_2$ oxidation starts with the breaking of the W−S bond, which is then followed by oxygen atoms displacing sulfur atoms at the surface.[28] The oxidized region has been identified as WO$_3$.[29] Oxygen and water molecules present would induce degradation.[30]

Often the degradation and decomposition of TMDs can be attributed to exposure to oxygen. Oxygen dissociates into individual atoms and adsorbs on the surface of the TMD flakes. This degradation is limited at room temperature by the energy barrier for O$_2$ dissociation and chemisorption; therefore, TMDs are stable in an ambient environment.[31] In Figure 2 we see that the decomposition of uncovered WS$_2$ occurred at ∼673 K and higher in air. Using this, the energy barrier for O$_2$ combined dissociation and chemisorption (E_a) can be roughly estimated by setting $10^{-12}e^{-E_a/k_B T} \sim 1$ at 673 K,[32] using the pre-exponential factor in the transition-state theory by Nan et al.[32] for the physical and chemical adsorption of oxygen molecules on MoS$_2$. This gives ∼1.6 eV, which is the same as that calculated by DFT.[31]

Because WS$_2$ is largely unchanged at 673 K in air when it is covered by h-BN, it is largely stabilized by h-BN encapsulation at high temperature (though the postcycle PL is still affected). The effectiveness of the h-BN encapsulation is not related to h-BN thickness (15−40 nm here) because the energy barrier for an O$_2$ molecule across a monolayer van der Waals layer by quantum tunneling is very high, 5 eV.[33] Instead, the imperfect passivation of h-BN covering the TMD is attributed to O$_2$ molecule penetration between the h-BN overlayer and the SiO$_2$ substrate surface, as in a previous study of van der Waals layer covering and passivating nanoparticle monolayers from oxidant gases,[34] which found an effective diffusion coefficient for 2D transport of O$_2$ underneath the van der Waals layer of ∼10^{-10} cm^2/s.[34] This might be due to the roughness and dangling bonds on the SiO$_2$ substrate surface, which would allow some molecules, such as O$_2$ and H$_2$O, to move here between the h-BN layer and SiO$_2$ substrate surface. Therefore, even if the covered sample is not seen to decompose, the transport of oxygen underneath the h-BN overlayer can degrade the PL measured after the heating cycle, and even more so for higher temperatures, longer heating cycles, and smaller area h-BN overlayers.

This mechanism could also help explain why covered WS$_2$ shows the lowest postcycle PL signal after heating in forming gas. The H$_2$ in forming gas likely moves faster across the h-BN/SiO$_2$ interface than these other, larger molecules used in the studies and apparently leads to defects in the covered monolayer WS$_2$. The trion peaks originate from doping level changes caused by charge defects generated by H$_2$ molecules. In contrast, forming gas leads to the least macroscopic decomposition of uncovered WS$_2$ of the gas environments examined.

As noted above, after the heating/cooling cycle to 773 K in air, the peak position of PL of h-BN-covered WS$_2$ showed a small red shift of 12 meV, which corresponds to an increase in the biaxial in-plane tensile strain of ∼0.12% if all due to strain.[25] Because WS$_2$ monolayers have a larger thermal expansion coefficient than does either Si or h-BN, an increase in this strain during the cooling cycle is expected (with

adhesion between either WS$_2$ and the substrate (of ∼0.21−0.35%) or between WS$_2$ and h-BN (∼0−0.13%), with the range due to the uncertainty in the WS$_2$ ML thermal expansion coefficient).[35−37] The integrated PL at room temperature decreases after this cycle in air by ∼63%. This large amount of decrease cannot be attributed to this strain change. Lloyd et al. measured the integrated PL intensity change as a function of biaxial in-plane tensile strain and found that an ∼0.12% increase in biaxial in-plane tensile strain corresponds to a decrease in PL integrated intensity of ∼9%.[38] Thermal damage could be important for PL quenching, including some of it possibly being linked to the spots seen in Figure 3.

The overall PL blue shift with flowing N$_2$ and forming gas would indicate additional factors beyond strain, such as changes in doping and the lattice parameters. This would be expected with electron concentration increases[39] and molecular bonding to sulfur vacancies.[40] This could indicate thermal damage in both cases, the more so with forming gas, which had the much larger PL blue shift and decrease in PL intensity.

The temperature dependence of the integrated PL intensity and the fwhm in ambient air are fit in parts (a) and (b), respectively, of Figure 5. The fwhm line width of the PL, due
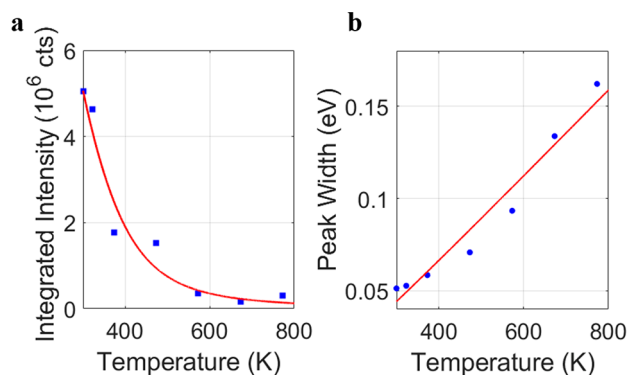
Figure 5. (a) Integrated PL intensity and (b) fwhm of h-BN-covered WS$_2$ flakes versus T under ambient air. The blue spots are the experimental data from the heating cycle run in Figure 2d. The red solid red line in (a) is a fitted curve and in (b) the peak fwhm fit with eq 1.

to exciton recombination in monolayer WS$_2$, depends on T as[41−44]

$$\Gamma(T) = \sigma T + \gamma N + \Gamma_0 \tag{1}$$

The first term comes from the acoustic phonon−exciton interaction, with the acoustic phonon coupling strength σ typically having an order of magnitude of a few μeV/K. The second term arises from the exciton−optical phonon interaction, and above 100 K its contribution is much larger than that of the first term. This second term is proportional to the number of phonons, as given by the Bose−Einstein distribution function:

$$N = \frac{1}{\exp\left(\frac{E}{k_B T}\right) - 1} \tag{2}$$

Here, E is the (weighted average) energy of the relevant phonons. γ is the optical phonon coupling strength. E, γ, and Γ_0 parameters are obtained by fitting the curve for PL fwhm in Figure 2d for heating of covered h-BN in ambient air. The "average" phonon energy is E = 25 meV, the exciton phonon

coupling strength is γ = 67.6 meV, and the temperature-independent broadening Γ_0 = 2 meV. These parameters are quite similar to those for MoS_2 in ref 43.

The dependence of the integrated PL signal on T is usually described by the following equation, which includes the quenching by two nonradiative recombination centers:[45−48]

$$I(T) = \frac{I_0}{1 + A \exp\left(-\frac{E_1}{k_B T}\right) + B \exp\left(-\frac{E_2}{k_B T}\right)} \quad (3)$$

(Supporting Information, Section S5). Parameters A and B represent the ratio of the nonradiative recombination rate to the radiative recombination rate for the two nonradiative recombination centers, and E_1 and E_2 represent the thermal activation energies for PL quenching for each one. For the PL intensity in Figure 2a of covered h-BN in ambient air, the activation energies are E_1 = 51.2 meV and E_2 = 229 meV, and A = 54 and B = 10 160. Because the binding energy of free excitons in monolayer WS_2 is 320 meV,[42] the larger energy E_2 is thought to be the energy needed to unbind bound excitons in WS_2. The lower energy E_1 represents the activation energy of exciton diffusion to the vicinity of local nonradiative recombination centers.[48] Nonradiative recombination dominates radiative decay at all studied T and does so increasingly at higher T. In the lower T range studied, exciton diffusion is more important than exciton unbinding, whereas in the higher temperature range, exciton unbinding dominates.

The PL intensity during the heating of covered WS_2 in N_2 of Figure 4b is also fit; similar parameters are obtained as those for air, as seen in the Supporting Information (Figure S6). It is not fit for covered WS_2 heated in forming gas because of the noted PL damage in that case.

A trion peak is seen in the PL during the cooling of covered h-BN with flowing forming gas at and below 323 K (Figure 4c). The trion binding energy is very roughly estimated to be $k_B T$ at the temperature it first appears (323 K), which is approximately 28 meV. This corresponds well to the findings of a previous PL study of WS_2, which was conducted down to 4 K, 20−30 meV.[42]

CONCLUSIONS

CVD-grown triangular-shape high-quality monolayers of WS_2 can be well stabilized at elevated temperatures by encapsulation with several-layer h-BN, but to different degrees in the presence of ambient air, flowing N_2, or flowing forming gas (95% N_2, 5% H_2). The best passivation occurs for h-BN-covered samples with flowing N_2, as judged by the PL intensity after the cycle, which decreases the least with that gas. Furthermore, no degradation of the covered WS_2 flakes is seen visually in N_2 up to the highest tested examined temperature, 873 K. This might be due to "minimal" O_2 and H_2O molecules. Spots are seen to form in the middle of the flakes after heating in ambient air, but not after heating in N_2. Postcycle PL is weakest for forming gas, presumably due to the damage by the rapid H_2 diffusion between the h-BN and SiO_2 substrate surface. For forming gas only, trion PL peaks are seen, and they are seen near the end of the cooldown cycle. Also, macroscopic degeneration of the covered WS_2 is seen in forming gas at high temperatures. In contrast, flowing forming gas leads to the least macroscopic degeneration of uncovered WS_2 at elevated temperature. One would expect WS_2 flakes would be passivated even better with h-BN encapsulation on the top and bottom, and in the presence of N_2.

ASSOCIATED CONTENT

Supporting Information

The Supporting Information is available free of charge at https://pubs.acs.org/doi/10.1021/acsami.1c06348.

More details of the experimental setup; room-temperature Raman scattering and photoluminescence in flowing nitrogen and forming gas; Raman scattering before and after heating in flowing forming gas; optical micrographs before and after heating in flowing nitrogen; temperature dependence of photoluminescence; fitting the temperature dependence of photoluminescence in flowing nitrogen (PDF)

AUTHOR INFORMATION

Corresponding Author

Irving P. Herman − Department of Applied Physics and Applied Mathematics, Columbia University, New York 10027, United States; orcid.org/0000-0001-8492-6000; Email: iph1@columbia.edu

Authors

Xiang Hua − Department of Applied Physics and Applied Mathematics, Columbia University, New York 10027, United States; orcid.org/0000-0001-8834-5932

Datong Zhang − Department of Applied Physics and Applied Mathematics, Columbia University, New York 10027, United States; orcid.org/0000-0003-4062-5913

Bumho Kim − Department of Mechanical Engineering, Columbia University, New York 10027, United States

Dongjea Seo − Department of Materials Science and Engineering, Yonsei University, Seoul 120-749, Korea; Department of Electrical and Computer Engineering, University of Minnesota, Minneapolis, Minnesota 55455, United States

Kyungnam Kang − Department of Mechanical Engineering, Stevens Institute of Technology, Hoboken, New Jersey 07030, United States

Eui-Hyeok Yang − Department of Mechanical Engineering, Stevens Institute of Technology, Hoboken, New Jersey 07030, United States; orcid.org/0000-0003-4893-1691

Jiayang Hu − Department of Applied Physics and Applied Mathematics, Columbia University, New York 10027, United States; orcid.org/0000-0001-6707-1549

Xianda Chen − Department of Applied Physics and Applied Mathematics, Columbia University, New York 10027, United States

Haoran Liang − Department of Applied Physics and Applied Mathematics, Columbia University, New York 10027, United States

Kenji Watanabe − Advanced Materials Laboratory and Research Center for Functional Materials, National Institute for Materials Science, Tsukuba 305-0044, Japan; orcid.org/0000-0003-3701-8119

Takashi Taniguchi − Advanced Materials Laboratory and International Center for Materials Nanoarchitectonics, National Institute for Materials Science, Tsukuba 305-0044, Japan; orcid.org/0000-0002-1467-3105

James Hone − Department of Mechanical Engineering, Columbia University, New York 10027, United States

Young Duck Kim − Department of Physics, Department of Information Display, and KHU-KIST Department of Converging Science and Technology, Kyung Hee University,

Seoul 02447, Republic of Korea; ● orcid.org/0000-0003-2593-9826

Author Contributions

The paper was written through the contributions of all the authors. All authors have given approval to the final version of the paper.

Notes

The authors declare no competing financial interest.

■ REFERENCES

(1) Wang, Q. H.; Kalantar-Zadeh, K.; Kis, A.; Coleman, J. N.; Strano, M. S. Electronics and Optoelectronics of Two-Dimensional Transition Metal Dichalcogenides. *Nat. Nanotechnol.* **2012**, *7*, 699−712.

(2) Mak, K. F.; Lee, C.; Hone, J.; Shan, J.; Heinz, T. F. Atomically Thin MoS_2: A New Direct-Gap Semiconductor. *Phys. Rev. Lett.* **2010**, *105*, 136805.

(3) Splendiani, A.; Sun, L.; Zhang, Y.; Li, T.; Kim, J.; Chim, C.-Y.; Galli, G.; Wang, F. Emerging Photoluminescence in Monolayer MoS_2. *Nano Lett.* **2010**, *10*, 1271−1275.

(4) Wu, S.; Buckley, S.; Schaibley, J. R.; Feng, L.; Yan, J.; Mandrus, D. G.; Hatami, F.; Yao, W.; Vučković, J.; Majumdar, A.; Xu, X. Monolayer Semiconductor Nanocavity Lasers with Ultralow Thresholds. *Nature* **2015**, *520*, 69−72.

(5) Palacios-Berraquero, C.; Barbone, M.; Kara, D. M.; Chen, X.; Goykhman, I.; Yoon, D.; Ott, A. K.; Beitner, J.; Watanabe, K.; Taniguchi, T.; Ferrari, A. C.; Atatüre, M. Atomically Thin Quantum Light-Emitting Diodes. *Nat. Commun.* **2016**, *7*, 12978.

(6) Yin, Z.; Li, H.; Li, H.; Jiang, L.; Shi, Y.; Sun, Y.; Lu, G.; Zhang, Q.; Chen, X.; Zhang, H. Single-Layer MoS_2 Phototransistors. *ACS Nano* **2012**, *6*, 74−80.

(7) Lopez-Sanchez, O.; Lembke, D.; Kayci, M.; Radenovic, A.; Kis, A. Ultrasensitive Photodetectors Based on Monolayer MoS_2. *Nat. Nanotechnol.* **2013**, *8*, 497−501.

(8) Baugher, B. W.; Churchill, H. O.; Yang, Y.; Jarillo-Herrero, P. Optoelectronic Devices based on Electrically Tunable pn Diodes in a Monolayer Dichalcogenide. *Nat. Nanotechnol.* **2014**, *9*, 262−267.

(9) Ross, S.; Sussman, A. Surface Oxidation of Molybdenum Disulfide. *J. Phys. Chem.* **1955**, *59*, 889−892.

(10) Cannon, P. Melting Point and Sublimation of Molybdenum Disulphide. *Nature* **1959**, *183*, 1612−1613.

(11) Cho, S.; Kim, S.; Kim, J. H.; Zhao, J.; Seok, J.; Keum, D. H.; Baik, J.; Choe, D.-H.; Chang, K. J.; Suenaga, K.; Kim, S. W.; Lee, Y. H.; Yang, H. Phase Patterning for Ohmic Homojunction Contact in $MoTe_2$. *Science* **2015**, *349*, 625−628.

(12) Lin, J.; Pantelides, S. T.; Zhou, W. Vacancy-Induced Formation and Growth of Inversion Domains in Transition-Metal Dichalcogenide Monolayer. *ACS Nano* **2015**, *9*, 5189−5197.

(13) Yamamoto, M.; Dutta, S.; Aikawa, S.; Nakaharai, S.; Wakabayashi, K.; Fuhrer, M. S.; Ueno, K.; Tsukagoshi, K. Self-Limiting Layer-by-Layer Oxidation of Atomically Thin WSe_2. *Nano Lett.* **2015**, *15*, 2067−2073.

(14) Ueno, K.; Fukushima, K. Changes in Structure and Chemical Composition of α-$MoTe_2$ and β-$MoTe_2$ During Heating in Vacuum Conditions. *Appl. Phys. Express* **2015**, *8*, 095201.

(15) Wang, D.; Smyser, K.; Rhodes, D.; Balicas, L.; Pasupathy, A.; Herman, I. P. Passivating 1T'-$MoTe_2$ Multilayers at Elevated Temperatures by Encapsulation. *Nanoscale* **2017**, *9*, 13910−13914.

(16) Wu, Z.; Luo, Z.; Shen, Y.; Zhao, W.; Wang, W.; Nan, H.; Guo, X.; Sun, L.; Wang, X.; You, Y.; Ni, Z. Defects as a Factor Limiting Carrier Mobility in WSe_2: A Spectroscopic Investigation. *Nano Res.* **2016**, *9*, 3622−3631.

(17) Liu, Z.; Gong, Y.; Zhou, W.; Ma, L.; Yu, J.; Idrobo, J. C.; Jung, J.; MacDonald, A. H.; Vajtai, R.; Lou, J.; Ajayan, P. M. Ultrathin High-Temperature Oxidation-Resistant Coatings of Hexagonal Boron Nitride. *Nat. Commun.* **2013**, *4*, 2541.

(18) Ajayi, O. A.; Ardelean, J. V.; Shepard, G. D.; Wang, J.; Antony, A.; Taniguchi, T.; Watanabe, K.; Heinz, T. F.; Strauf, S.; Zhu, X. Y.; Hone, J. C. Approaching the Intrinsic Photoluminescence Linewidth in Transition Metal Dichalcogenide Monolayers. *2D Mater.* **2017**, *4*, 031011.

(19) Kim, Y. D.; Gao, Y.; Shiue, R.-J.; Wang, L.; Aslan, O. B.; Bae, M.-H.; Kim, H.; Seo, D.; Choi, H.-J.; Kim, S. H.; Nemilentsau, A.; Low, T.; Tan, C.; Efetov, D. K.; Taniguchi, T.; Watanabe, K.; Shepard, K. L.; Heinz, T. F.; Englund, D.; Hone, J. Ultrafast Graphene Light Emitters. *Nano Lett.* **2018**, *18*, 934−940.

(20) Kang, K. N.; Godin, K.; Yang, E.-H. The Growth Scale and Kinetics of WS_2 Monolayers Under Varying H_2 Concentration. *Sci. Rep.* **2015**, *5*, 13205.

(21) Wang, L.; Meric, I.; Huang, P. Y.; Gao, Q.; Gao, Y.; Tran, H.; Taniguchi, T.; Watanabe, K.; Campos, L. M.; Muller, D. A.; Guo, J.; Kim, P.; Hone, J.; Shepard, K. L.; Dean, C. R. One-Dimensional Electrical Contact to a Two-Dimensional Material. *Science* **2013**, *342*, 614.

(22) Zhu, C. R.; Wang, G.; Liu, B. L.; Marie, X.; Qiao, X. F.; Zhang, X.; Wu, X. X.; Fan, H.; Tan, P. H.; Amand, T.; Urbaszek, B. Strain Tuning of Optical Emission Energy and Polarization in Monolayer and Bilayer MoS_2. *Phys. Rev. B: Condens. Matter Mater. Phys.* **2013**, *88*, 121301.

(23) Shi, H.; Pan, H.; Zhang, Y.-W.; Yakobson, B. I. Quasiparticle Band Structures and Optical Properties of Strained Monolayer MoS_2 and WS_2. *Phys. Rev. B: Condens. Matter Mater. Phys.* **2013**, *87*, 155304.

(24) Island, J. O.; Kuc, A.; Diependaal, E. H.; Bratschitsch, R.; van der Zant, H. S. J.; Heine, T.; Castellanos-Gomez, A. Precise and Reversible Band Gap Tuning in Single-Layer $MoSe_2$ by Uniaxial Strain. *Nanoscale* **2016**, *8*, 2589−2593.

(25) Frisenda, R.; Drüppel, M.; Schmidt, R.; Michaelis de Vasconcellos, S.; Perez de Lara, D.; Bratschitsch, R.; Rohlfing, M.; Castellanos-Gomez, A. Biaxial strain tuning of the optical properties of single-layer transition metal dichalcogenides. *npj 2D Mater. Appl.* **2017**, *1*, 10.

(26) Lauritsen, J. V.; Nyberg, M.; Vang, R. T.; Bollinger, M. V.; Clausen, B. S.; Topsoe, H.; Jacobsen, K. W.; Laegsgaard, E.; Norskov, J. K.; Besenbacher, F. Chemistry of One-Dimensional Metallic Edge States in MoS_2 Nanoclusters. *Nanotechnology* **2003**, *14*, 385−389.

(27) Peterson, S. L.; Schulz, K. H. Ethanethiol Decomposition Pathways on $MoS_2(0001)$. *Langmuir* **1996**, *12*, 941−945.

(28) Gao, J.; Li, B.; Tan, J.; Chow, P.; Lu, T.-M.; Koratkar, N. Aging of Transition Metal Dichalcogenide Monolayers. *ACS Nano* **2016**, *10*, 2628−2635.

(29) Kang, K.; Godin, K.; Kim, Y. D.; Fu, S.; Cha, W.; Hone, J.; Yang, E.-H. Graphene-Assisted Antioxidation of Tungsten Disulfide Monolayers: Substrate and Electric-Field Effect. *Adv. Mater.* **2017**, *29*, 1603898.

(30) Budania, P.; Baine, P.; Montgomery, J.; McGeough, C.; Cafolla, T.; Modreanu, M.; McNeill, D.; Mitchell, N.; Hughes, G.; Hurley, P. Long-Term Stability of Mechanically Exfoliated MoS_2 Flakes. *MRS Commun.* **2017**, *7*, 813−818.

(31) Martincová, J.; Otyepka, M.; Lazar, P. Is Single Layer MoS_2 Stable in the Air? *Chem. - Eur. J.* **2017**, *23*, 13233−13239.

(32) Nan, H.; Wang, Z.; Wang, W.; Liang, Z.; Lu, Y.; Chen, Q.; He, D.; Tan, P.; Miao, F.; Wang, X.; Wang, J.; Ni, Z. Strong Photoluminescence Enhancement of MoS_2 through Defect Engineering and Oxygen Bonding. *ACS Nano* **2014**, *8*, 5738−5745.

(33) Sen, H. S.; Sahin, H.; Peeters, F. M.; Durgun, E. Monolayers of MoS_2 as an Oxidation Protective Nanocoating Material. *J. Appl. Phys.* **2014**, *116*, 083508.

(34) Zhang, D.; Wang, D. Z.-R.; Creswell, R.; Lu, C.; Liou, J.; Herman, I. P. Passivation of CdSe Quantum Dots by Graphene and MoS_2 Monolayer Encapsulation. *Chem. Mater.* **2015**, *27*, 5032−5039.

(35) McCreary, K. M.; Hanbicki, A. T.; Singh, S.; Kawakami, R. K.; Jernigan, G. G.; Ishigami, M.; Ng, A.; Brintlinger, T. H.; Stroud, R. M.; Jonker, B. T. The Effect of Preparation Conditions on Raman and Photoluminescence of Monolayer WS_2. *Sci. Rep.* **2016**, *6*, 35154.

(36) Singh, S. K.; Neek Amal, M.; Costamagna, S.; Peeters, F. M. Thermomechanical Properties of a Single Hexagonal Boron Nitride Sheet. *Phys. Rev. B: Condens. Matter Mater. Phys.* **2013**, *87*, 184106.

(37) Okada, Y.; Tokumaru, Y. Precise Etermination of Lattice Parameter and Thermal Expansion Coefficient of Silicon between 300 and 1500 K. *J. Appl. Phys.* **1984**, *56*, 314−320.

(38) Lloyd, D.; Liu, X.; Christopher, J. W.; Cantley, L.; Wadehra, A.; Kim, B. L.; Goldberg, B. B.; Swan, A. K.; Bunch, J. S. Band Gap Engineering with Ultralarge Biaxial Strains in Suspended Monolayer MoS_2. *Nano Lett.* **2016**, *16*, 5836−5841.

(39) Mak, K. F.; He, K.; Lee, C.; Lee, G. H.; Hone, J.; Heinz, T. F.; Shan, J. Tightly Bound Trions in Monolayer MoS_2. *Nat. Mater.* **2013**, *12*, 207−211.

(40) Kim, H.-J.; Yun, Y. J.; Yi, S. N.; Chang, S. K.; Ha, D. H. Changes in the Photoluminescence of Monolayer and Bilayer Molybdenum Disulfide during Laser Irradiation. *ACS Omega* **2020**, *S*, 7903−7909.

(41) Rudin, S.; Reinecke, T. L. Temperature-Dependent Exciton Linewidths in Semiconductor Quantum Wells. *Phys. Rev. B: Condens. Matter Mater. Phys.* **1990**, *41*, 3017−3027.

(42) Chernikov, A.; Berkelbach, T. C.; Hill, H. M.; Rigosi, A.; Li, Y.; Aslan, O. B.; Reichman, D. R.; Hybertsen, M. S.; Heinz, T. F. Exciton Binding Energy and Nonhydrogenic Rydberg Series in Monolayer WS_2. *Phys. Rev. Lett.* **2014**, *113*, 076802.

(43) Cadiz, F.; Courtade, E.; Robert, C.; Wang, G.; Shen, Y.; Cai, H.; Taniguchi, T.; Watanabe, K.; Carrere, H.; Lagarde, D.; Manca, M.; Amand, T.; Renucci, P.; Tongay, S.; Marie, X.; Urbaszek, B. Excitonic Linewidth Approaching the Homogeneous Limit in MoS_2 Based van der Waals Heterostructures. *Phys. Rev. X* **2017**, *7*, 021026.

(44) Cheng, O. H.-C.; Qiao, T.; Sheldon, M.; Son, D. H. Size- and Temperature-Dependent Photoluminescence Spectra of Strongly Confined $CsPbBr_3$ Quantum Dots. *Nanoscale* **2020**, *12*, 13113−13118.

(45) Chia, C. H.; Yuan, C. T.; Ku, J. T.; Yang, S. L.; Chou, W. C.; Juang, J. Y.; Hsieh, S. Y.; Chiu, K. C.; Hsu, J. S.; Jeng, S. Y. Temperature Dependence of Excitonic Emission in Cubic CdSe Thin Film. *J. Lumin.* **2008**, *128*, 123−128.

(46) Leroux, M.; Grandjean, N.; Beaumont, B.; Nataf, G.; Semond, F.; Massies, J.; Gibart, P. Temperature Quenching of Photoluminescence Intensities in Undoped and Doped GaN. *J. Appl. Phys.* **1999**, *86*, 3721−3728.

(47) Tran, T. K.; Park, W.; Tong, W.; Kyi, M. M.; Wagner, B. K.; Summers, C. J. Photoluminescence Properties of ZnS Epilayers. *J. Appl. Phys.* **1997**, *81*, 2803−2809.

(48) Mukherjee, S.; Maiti, R.; Katiyar, A. K.; Das, S.; Ray, S. K. Novel Colloidal MoS_2 Quantum Dot Heterojunctions on Silicon Platforms for Multifunctional Optoelectronic Devices. *Sci. Rep.* **2016**, *6*, 29016.